

Deep non-invasive cerebral blood flow sensing using diffuse correlation spectroscopy and ATLAS

Quan Wang¹, Yuanyuan Hua², Chenxu Li¹, Mingliang Pan¹, Maciej Wojtkiewicz², Ahmet T. Erdogan², Alistair Gorman², Yuanzhe Zhang¹, Neil Finlayson², Yining Wang², Robert K. Henderson², and David Uei-Day Li^{1*}

¹University of Strathclyde, Faculty of Engineering, Department of Biomedical Engineering, Glasgow, UK.

²The University of Edinburgh, School of Engineering, Integrated Nano and Micro Systems (IMNS), Edinburgh, EH9 3JL, UK.

ABSTRACT:

Significance: Cerebral blood flow (CBF) is a crucial indicator of brain function, and continuous monitoring is critical for diagnosing and treating neurological disorders such as stroke, traumatic brain injury, and neurodegenerative diseases. Diffuse correlation spectroscopy (DCS) is a non-invasive diffuse optical technique to investigate deep tissue microvascular dynamics. However, traditional DCS systems face challenges in real-time applications due to reliance on correlation boards or software autocorrelators for signal acquisition, which limits their practical use. Additionally, most existing DCS measurements are confined to a source-detector separation, $\rho = 20 \sim 30$ mm, with a maximum $\rho \sim 40$ mm, potentially reducing cerebral hemodynamics assessment accuracy. To overcome these limitations, we utilized a fully in-house-built 512×512 single-photon avalanche diode array (SPAD) called ATLAS, featuring innovative on-chip autocorrelators.

Aim: This study evaluates the performance of the ATLAS-DCS system in liquid phantoms, cuff occlusion studies, and cerebral blood flow measurements.

Approach: The ATLAS-DCS system was compared against a commercial correlator board-based DCS system using liquid phantoms and cuff occlusion studies. For both ATLAS-DCS and conventional DCS, decorrelation time and decorrelation speed were calculated. To assess system performance, CBF was measured under normal conditions and during video gaming, leveraging the advantages of the chip-based correlator design and large pixel array.

Results: We successfully monitored pulsatile blood flow at ρ of 50 mm with a high sampling rate of up to 56.3 Hz in a human forehead *in vivo*. The system demonstrated high fidelity in detecting human pulse signals and identifying behaviour-induced physiological variations in the subject's prefrontal cortex during video gaming. We also showed that the ATLAS-DCS system outperforms the commonly used APD-based DCS system, achieving more than $571\times$ SNR improvement in a milk-phantom at ρ of 20 mm.

Conclusion: The ATLAS-DCS system enables reliable CBF measurements at larger source-detector separations and exhibits exceptional sensitivity to blood flow changes. This on-chip DCS design significantly enhances detection speed and sensitivity, paving the way for real-time, high-speed biological signal measurement in clinical and research application.

Keywords: SPAD, diffuse correlation spectroscopy, cerebral blood flow, on-chip correlator

*David Day-Uei Li, E-mail: david.li@strath.ac.uk

1. Introduction

Cerebral blood flow (CBF) is a critical indicator of brain health, revealing whether the brain receives sufficient oxygen and nutrients to maintain its functions¹. Irregular CBF can lead to severe neurological disorders, such as ischemic stroke^{2,3}, brain trauma^{4,5}, neurodegenerative diseases⁶, Alzheimer's^{7,8} and Parkinson's^{9,10}. CBF also reveals brain functionality, with neural activity prompting hemodynamic changes through neurovascular coupling mechanisms^{11–13}, reflecting how neuronal activation leads to localized blood flow (BF) variations. Monitoring CBF continuously and in real-time is desirable to enable timely intervention and devise a personalized treatment.

Diffuse optics technologies (including diffuse correlation spectroscopy (DCS)^{14,15}, laser Doppler flowmetry (LDF)¹⁶, laser speckle contrast imaging (LSCI)¹⁷, diffuse speckle contrast analysis (DSCA)^{18,19}, and speckle contrast optical spectroscopy (SCOS)^{20,21}) are non-invasive for microvascular BF measurements^{22–24}. Among them, DCS has gained considerable attention. Briefly, DCS measures the temporal fluctuations of scattered near-infrared light through biological tissues (e.g., the brain's cortex), achieving a deeper penetration depth than traditional imaging methods^{23,25,26}. DCS has been used to bedside-assess brain injuries^{27–30} and cancer therapies^{31–35}. Typically, the penetration depth is usually $1/3 \sim 1/2$ of the source-detector separation (ρ)²⁷. Traditionally, DCS utilizes single-mode or few-mode fibers to capture speckle patterns, combined with avalanche photodiodes (APD, e.g., SPCM-AQ4C)³⁶ to generate the intensity temporal auto-correlation function, $g_2(\tau)$ ²⁷. However, the low photon throughput from deeper tissues (at a larger ρ) gives a reduced signal-to-noise ratio (SNR) in BF measurements³⁷.

To address this limitation, highly integrated CMOS single photon avalanche diode (SPAD) sensors have been introduced in DCS research. Johansson *et al.* first used a 5×5 SPAD array to obtain an improved SNR in milk phantoms and *in vivo* blood perfusion tests³⁸, followed by a 32×32 SPAD array (Photon Force, Ltd.)^{39,40}, which provided a 32-fold increase in SNR. Then Rocca *et al.*⁴¹ used the 192×128 QuantiCAM SPAD sensor⁴² with on-FPGA autocorrelators to obtain the $g_2(\tau)$. In 2023, Michael *et al.* used a 500×500 SPAD array⁴³ in optical phantom studies. In 2024, Kreiss *et al.* used the same camera for *in vivo* experiments, measuring BF in human subjects at $\rho \sim 40$ mm with a fast sampling of pulsatile BF at 8-10 Hz. Roughly at the same time, Henderson's research group developed a 512×512 SPAD sensor called ATLAS^{44,45} with on-chip autocorrelators. A summary of SPAD camera-based DCS systems is provided in Table 1.

For autocorrelation calculations, most DCS systems use either a counter-acquisition board that counts detector output pulses and connects to a computer running a software correlator^{46,47}, or a commercial hardware correlator board²⁴ that performs both tasks. Software autocorrelators are highly adaptable and can be customized to compute physiologically relevant correlations

at specific delay times. However, they require high-performance computers for processing and can be time-intensive, particularly with high-frame-rate DCS data. Whereas commercial autocorrelators offer real-time g_2 calculations, they are less flexible and hard for end users to reconfigure.

To address these challenges, instead of relying on external field-programmable gate arrays (FPGAs) for real-time autocorrelation processing as done with general-purpose SPAD arrays⁴⁸, in the ATLAS-DCS system the correlator circuitry is directly integrated into the silicon of a 512×512 SPAD camera. This system supports two modes for DCS applications: “ensemble” mode, which averages the $g_2(\tau)$ curve across the entire frame for high-speed measurements, and DCS imaging mode, where $g_2(\tau)$ is calculated at individual pixel levels.

In this study, we utilized the ATLAS-DCS system to conduct measurements of cardiac pulse waveforms at $\rho > 45$ mm and assess human brain activity at $\rho = 30$ mm. We compared the proposed DCS system to conventional DCS systems, demonstrating a high sampling rate and SNR at a larger ρ . We present ATLAS’ exceptional performance in monitoring human BF and brain function with unprecedented signal quality at extended ρ . Specifically, it offers real-time blood flow monitoring (see the video in **Supplementary**) at a 56 Hz sampling rate while maintaining the accuracy and performing better than a conventional APD-based DCS system. These advancements present new opportunities for brain research and clinical applications.

Table 1 Existing SPAD camera-based DCS

Detector	Laser Wavelength (nm)	N pixel	applications	PDE	Fill factor	Frame rate (kHz/kfps)	ρ (m)	Way of analysis	Year	Refs
SPAD	785	5×5	Phantom, blood perfusion	8%	1.5%	1000	25	Off-line	2019	³⁸
SPAD	785	32×32	Diffuser, milk phantom	8%	1.5%	333	11	Off-line	2020	⁴⁰
SPAD	670	32×32	Phantom, forehead, neural activity	16%	1.5%	333	21	Off-line	2021	³⁹
SPAD	785	192×128	Diffuser	8%	13%	26		FPGA	2023	⁴¹
SPAD	785	500×500	Milk phantom	15%	10.6%	92.2	33	Off-line/FPGA	2023	⁴³
SPAD	785	500×500	Forearm, forehead	15%	10.6%	100 for arm, 300 for brain	40	Off-line	2024	⁴⁹
SPAD	785	512×512/128×128	Palm, forehead	47%	100%	27	50	Chip-based	2024	⁴⁴
SPAD	785	512×512/128×128	Forearm, forehead, neural activity	47%	100%	27	50	Chip-based	2024	This work

2. Methods

2.1 SPAD System

ATLAS was fabricated using 65/40 nm 3D-stacked CMOS technology, featuring a top-layer with a 512×512 array of deep trench isolated microlens SPADs with a $10.17 \mu\text{m}$ pitch. These SPADs achieve a peak photon detection efficiency (PDE) of 55% at 600 nm, and 26% at 940 nm, with a median dark count rate (DCR) of 500 counts per second at the room temperature under a 23 V bias (breakdown voltage of 17.8 V) ⁵⁰. ATLAS comprises a photosensitive array containing 128×128 macropixels and a column-parallel processing block. Each macropixel is capable of computing the photon counts $C\tau$ and accumulated photon counts $A\tau$ coefficients at 31 different time lags, utilizing an in-pixel shift register, multiplier, accumulator, and 32 banks of static random-access memory (SRAM). Each macropixel detects incident photons via 16 SPADs, whose outputs are combined and connected to a digital counter. The photon counts at each time lag are stored in a 32-element shift register. An in-pixel controller circuit manages the multiplier to calculate the $C\tau$ and $A\tau$ coefficients for the respective time lags, corresponding to the different shift register elements. These coefficients are stored in the in-pixel SRAM memory banks and then read out to the on-chip column-parallel processing circuits, where the g_2 coefficient, averaged across the entire macropixel array is calculated.

The operation of ATLAS requires two clocks provided by the FPGA: SYS_CLK, which serves as the main clock for the sensor, and PIX_CLK, which manages the macropixels' operations. Both clocks are derived using the mixed mode clock manager. Additionally, a few control signals are required to operate the sensor. The row address bits, ROW_ADDR<0:6>, and channel address bits, CHANNEL_ADDR<0:4> are used to select the desired row of macropixels and the corresponding bank of the in-pixel SRAM memory, respectively. The signals START_ACCUMULATE, START_DIVISION and G2_SUM_RST control the calculations of the g_2 coefficient within the column-parallel processing circuits.

The g_2 data is first read from ATLAS into a first-in-first-out (FIFO) block implemented in the FPGA and then stored in the DRAM. From there, it is transferred to the USB 3.0 microcontroller via another FIFO block, and finally, the data is sent to the PC through the USB 3.0 interface. Fig. 1 shows the configuration of the sensor.

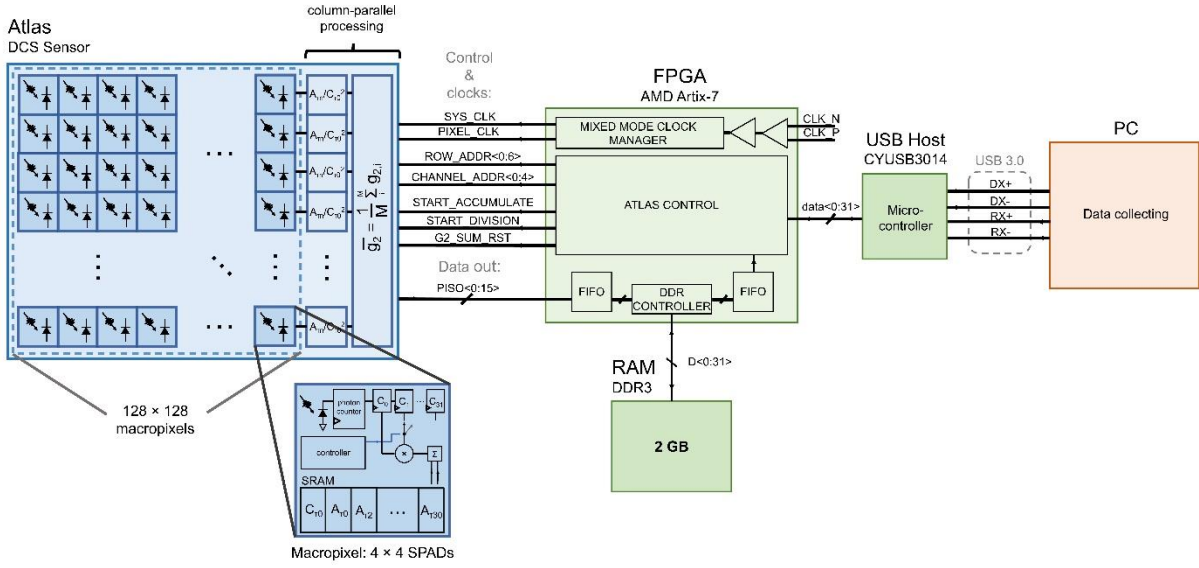


Fig. 1 Shows the DCS camera (using ATLAS) system architecture. ATLAS is controlled and read out by the field programmable gate array (FPGA), employing double data rate (DDR) 3 dynamic random-access memory (DRAM) for fast data acquisition and the USB 3.0 interface to communicate with a PC for data acquisition.

2.2 Theoretical Modelling

In DCS, the motion information of particles in the tissues is carried in the electric field of diffuse light $E(t)$. It can be extracted from the unnormalized electric field temporal auto-correlation function, which is defined as $G_1(\tau) \equiv \langle E(t)E^*(t + \tau) \rangle$, where $\langle \dots \rangle$ denotes temporal average. $G_1(\tau)$ can be modelled with the correlation diffusion equation⁵¹, giving a normalized solution, $g_1(\tau) = G_1(\tau)/G_1(\tau = 0)$, for a semi-infinite homogeneous geometry under the assumption of extrapolated boundary conditions⁵² as,

$$g_1(\tau) = \frac{r_2 \exp(-K_D(\tau)r_1) - r_1 \exp(-K_D(\tau)r_2)}{r_2 \exp(-K_D(0)r_1) - r_1 \exp(-K_D(0)r_2)} \quad (1)$$

where $K_D^2(\tau) = 3\mu_a\mu'_s + \alpha\mu'_s k_0^2 \langle \Delta r^2(\tau) \rangle$, μ_a and μ'_s are the absorption and reduced scattering coefficients, respectively. ρ is the distance between the source and detection fibers, α is the probability of photon scattering events from a moving scatterer, $k_0 = 2\pi n_0/\lambda$ is the wavenumber at the wavelength λ , where n_0 is the tissue refractive index. And $r_1 = (\rho^2 + z_0^2)^{1/2}$, $r_2 = (\rho^2 + (z_0 + 2z_b)^2)^{1/2}$, $z_0 = (\mu_a + \mu'_s)^{-1}$, and $z_b = \frac{2}{3\mu'_s} \frac{1+R_{eff}}{1-R_{eff}}$ with $R_{eff} = 1.4400n^{-2} + 0.7100n^{-1} + 0.6680 + 0.0636n$ being the effective reflection coefficient, which is determined by the ratio of the refraction indices of two media (e.g., $n = \frac{n_0}{n_{air}} \approx 1.33$, n_{air} is the air refraction index). In practice, the mean square displacement, $\langle \Delta r^2(\tau) \rangle$, of the scattering particles in the lag time (τ) can be approximated by the Brownian motion model that shows better fitting in most applications, ranging from muscles to the brain. Thus $\langle \Delta r^2(\tau) \rangle = 6D_b\tau$, where D_b is the effective diffusion coefficient and the product αD_b commonly used as the DCS blood flow index (BFI).

To perform a DCS measurement, $g_2(\tau)$ was calculated at each macropixel SPAD pixel:

$$g_2^j(\tau) = \frac{\langle I_j(t) \cdot I_j(t+\tau) \rangle}{\langle I_j(t) \rangle^2}, \quad (2)$$

where $I_j(t)$ is the number of detected photons of the j -th SPAD pixel at a given time t . Then the final system autocorrelation function was calculated across $j = 1$ to N ; N is the number of SPAD pixels used for the measurements,

$$\bar{g}_2(\tau)|_N = \frac{1}{N} \sum_{j=1}^N g_2^j(\tau). \quad (3)$$

The normalized intensity ACF, $\bar{g}_2(\tau)$ is linked to the normalized electric field ACF, $g_1(\tau)$ through the Siegert relation⁵³:

$$g_2(\tau) = 1 + \beta |g_1(\tau)|^2, \quad (4)$$

where β is the coherence parameter.

In DCS experiments, the dynamic scattering media usually consist of scatterers exhibiting either random flow (ballistic) or Brownian (diffusive) motions. To obtain the decorrelation lifetime⁵⁴, τ_c , a simpler functional expression is preferred for fitting measured $\bar{g}_2(\tau)$:

$$f(\tau) = 1 + a \cdot \exp(-\nu\tau) \quad (5)$$

We define $\tau_c = 2/\nu$, where the coefficient ν of the exponential term is referred to as the “decorrelation speed” as adopted from Liu *et al.*³⁹. The decorrelation speed, directly related to blood flow velocity, reveals the pulsatile nature of the flow, indicated by periodic peaks in the time series. The blood flow index (BFI) is proportional to $1/\tau_c$ ¹⁷. Variations to τ_c can then be directly attributed to, for example, a change in blood flow.

2.3 Optical Setup

We conducted phantom and BF measurements using the proposed system and a conventional DCS system, as shown in Fig. 2. A continuous-wave (CW) laser (CrystaLaser, USA) with a wavelength $\lambda = 785$ nm was coupled into a multimode optical fiber (MMF; M143L01, core diameter = Ø200 µm, NA = 0.39, Thorlabs) through a collimator ($f = 6.24$ mm, NA = 0.37, Thorlabs), serving as the illuminating source. The coupling efficiency was 88.9%. The laser’s coherence length (> 10 m) was much longer than typical photon pathlengths, and its maximum output power was 120 mW. To attenuate the laser beam output to 30 mW, meeting ANRS safety requirements, a variable neutral density filter (NE205B, OD = 0.5, Thorlabs, UK) was placed between the laser and the source fiber tip. A single-mode fiber (P1-780A-FC-1, 780 - 970 nm, FC/PC, Ø3 mm jacket, 1 m long, Thorlabs) collected the scattered photons from the tissue. The distal end of the fiber was secured in a 5-axis optical mount (K5X1, Thorlabs) to control the distance between the fiber tip and the camera sensor (C13366GD, Hamamatsu, MPPC module). The detector output and the 25MHz external synchronization signal were directed to a photon correlator board (SPC-QC-140, Becker & Hickl, Germany) with a time resolution of 2.048 ns to compute the \bar{g}_2 function, which provides insights into the dynamics of scatterers, primarily red blood cells, within the probed region⁵⁵.

The ATLAS-DCS system, illustrated in Fig. 2, shares the laser source. Multiple-scattered light was collected by a multimode fiber (MMF; M59L01, core diameter = Ø1000 µm, NA = 0.39,

Thorlabs) placed at a separation distance ρ away from the source, then coupled to the ATLAS camera. The fiber tip at the detection path was mounted on a fiber adapter (SM05SMA, Thorlabs) and attached to a 5-axis optic mount (K5X1, Thorlabs) to control the spacing between the tip and camera sensor. The sensor was fixed on the optical table, and the illuminating light intensity was adjusted to 30 mW, as verified by a power meter (LASERPOINT, Italy).

The average diameter of a speckle can be obtained using the following equation⁵⁶:

$$d_s = \frac{\lambda y}{D}, \quad (6)$$

where $\lambda = 785$ nm, y is the distance between the detection fiber end and the SPAD camera, and D is the core diameter of the detection fiber (1000 μm). We calibrated our system by adjusting y in the setup to align the light cone from the detector fiber with the entire detector array. This optimization maximized collected light while avoiding excessively high light intensity, which could cause saturation or nonlinear effects in the autocorrelation. We obtained the optimized fiber-SPAD distance $y \approx 12$ mm. During the measurement, the photon detection information is streamed to Opal Kelly XEM7310-A200 FPGA.

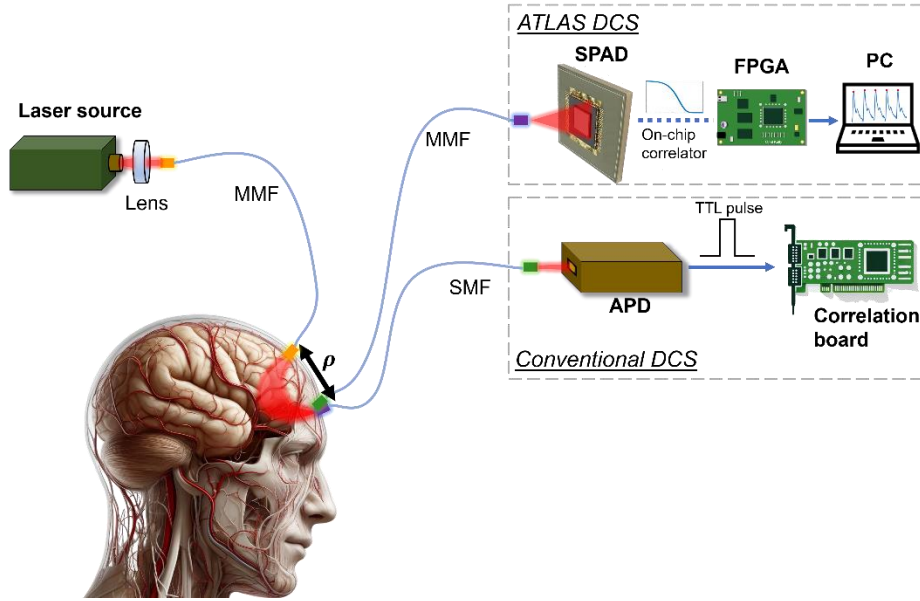


Fig. 2. Schematic of the Conventional and ATLAS-DCS instrumentation in the tissues. A highly coherent, long-coherence-length laser illuminates the sample via a multimode fiber (MMF). The motion of red blood cells induces fluctuations in the intensity of backscattered light, collected at a separation distance ρ from the source. In the conventional DCS system, the scattered light is routed to the Hamamatsu sensor via a single-mode fiber (SMF), and a correlator counts the arrival of digital TTL pulses generated by the sensor to compute the g_2 . In the ATLAS-DCS system, a PCB board hosts an Opal Kelly XEM7310-A200 FPGA. Note: The human head in the figure was generated using ChatGPT.

2.4 Data Processing

Fig. 3 illustrates the comparison between conventional and ATLAS-DCS data analysis pipelines. In the conventional DCS approach (Fig. 3(a)), photon counts are accumulated using macro time stamps within specified time windows (e.g., 0.75×10^{-6} s), resulting in intensity

time traces. These traces are used to compute $g_2(\tau)$, which characterizes the decay of correlation over time and provides insights into the decorrelation speed of the measured signal. While effective, this method requires off-chip processing, making it computationally intensive, impossible for real-time analysis.

In contrast, the ATLAS-DCS solution (Fig. 3(b)) integrates data acquisition and processing on-chip, enabling efficient, ensemble-mode (or DCS imaging mode) computation of $g_2(\tau)$ at a high speed (56.3 Hz). This enables real-time monitoring of dynamic processes without extensive post-processing, ideal for applications demanding immediate feedback, such as real-time BF monitoring for cardiovascular surgeries⁵⁷. By reducing latency and computational burden, ATLAS-DCS represents a significant advancement in dynamic light scattering.

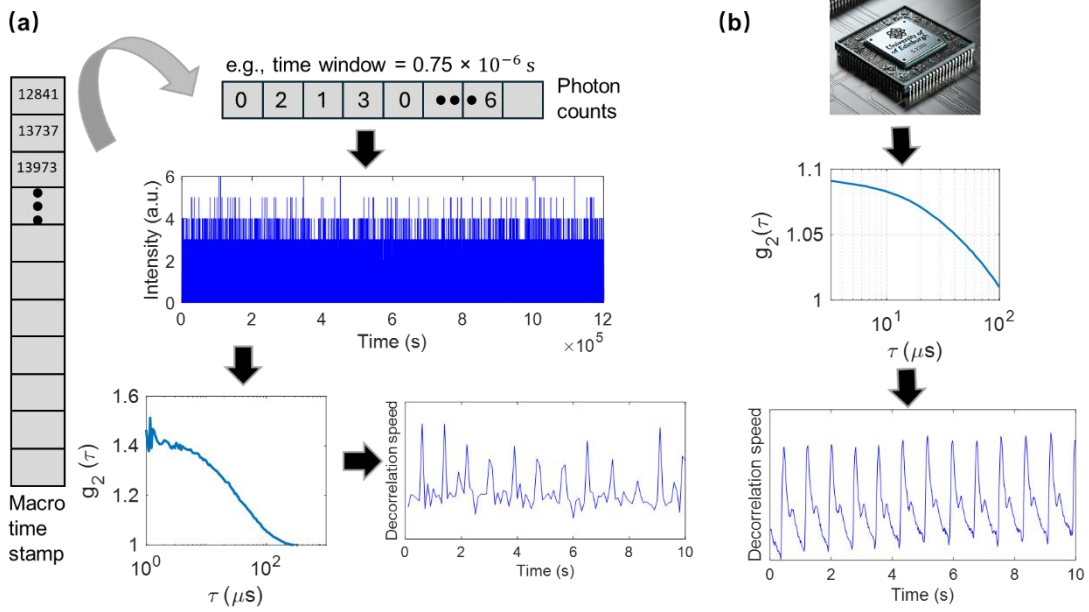


Fig. 3. The comparison of conventional DCS and ATLAS-DCS data analysis pipelines. (a) Conventional DCS: Photon counts are collected using macro time stamps in defined time windows (e.g., 0.75×10^{-6} s), resulting in intensity time traces. These traces are used to calculate $g_2(\tau)$, which provides information about the decorrelation speed over time. All these processes are performed offline. (b) ATLAS-DCS: An integrated approach where data is processed on-chip, yielding $g_2(\tau)$ in the ensemble mode (or the DCS imaging mode) and the corresponding decorrelation speed more efficiently, enabling real-time monitoring of dynamic processes.

3. Results

3.1. System Evaluation

To validate our conventional DCS system, we used a milk-phantom (3.7% Fat, Tesco, Glasgow, UK) at room temperature (approximately 20 °C) at $\rho = 20$ mm. The DCS measurements were performed using the liquid phantom setup shown in Fig. 4(a). Fig. 4(b) displays measured $g_2(\tau)$ with an integration time of 0.1s (the sampling rate = 10 Hz). The results show a faster decay for pure milk (blue curve), with progressively slower decay as water is added. This trend is expected, as adding water reduces scattering intensity and alters dynamics, slowing the correlation function decay. A faster decay in $g_2(\tau)$ usually corresponds to smaller particles or faster scatterer motions (fat globules in this case), consistent with the higher milk concentration. For the fitting, the pure milk (no added water) was assumed to have $n = 1.33$, $\mu_a = 0.001 \text{ mm}^{-1}$.

¹, and $\mu'_s = 2.3 \text{ mm}^{-1}$ ⁵⁸. For a milk-to-water ratio of 1:3, $\mu_a = 0.0033 \text{ mm}^{-1}$ and $\mu'_s = 0.81 \text{ mm}^{-1}$, whereas for a ratio of 1:5, $\mu_a = 0.0033 \text{ mm}^{-1}$, and $\mu'_s = 0.41 \text{ mm}^{-1}$ ⁴³. The measured $g_2(\tau)$ were fitted to Eqs. (1) and (4) to obtain a diffuse coefficient (αD_b) using a non-linear least squares optimization algorithm in MATLAB (Mathworks, USA), as shown in Fig. 4(c). In Fig. 4(c), the grey line (the milk-to-water ratio was 1:5) exhibits the highest αD_b , fluctuating between 1.0×10^{-6} to $1.7 \times 10^{-6} \text{ mm}^2 \cdot \text{s}^{-1}$. This behavior aligns with expectations, as higher water content disperses fat globules and allows freer particle movement, increasing αD_b . Conversely, the blue line (pure milk) shows the lowest αD_b , ranging from 0.3×10^{-6} to $1.0 \times 10^{-6} \text{ mm}^2 \cdot \text{s}^{-1}$. This is because the increased concentration of fat globules in the mixture intensifies interactions, further slowing particle motion.

Contrary to what we expected, αD_b for pure milk (blue) is lower than the diluted milk mixtures. This outcome can be explained by considering that αD_b not only depends on particle motion but also on the scatterer density. In pure milk, the scattering is stronger. Although the motion may be faster, the signal may saturate faster due to multiple scattering events. In diluted milk (1:3 or 1:5), fewer scattering events lead to a clearer representation of movement, which can result in a higher αD_b . Pure milk has the highest concentration of fat globules, resulting in more particle interactions and greater hindrance to motion, leading to a lower αD_b . Thus, this discrepancy arises due to the interplay between scattering events and particle motions, not just the speed of decorrelation alone, which agrees with the results reported in Ref.⁵⁹. All the curves show some fluctuations in αD_b over time, a common occurrence in such experiments, likely due to measurement noise or dynamic changes in particle motion. This experiment confirms our conventional DCS system's performance, which was used as a benchmark.

Next, we collected data simultaneously using the conventional and ATLAS-DCS system for a thorough comparison. The measured $g_2(\tau)$ s were fitted to Eq. (5) to determine the decorrelation time over 30 seconds, as shown in Fig. 4(d). The decorrelation time from the conventional DCS system remained nearly constant over the 30 s measurement window, with a mean value of $81.39 \pm 81.39 \text{ } \mu\text{s}$. In comparison, the ATLAS-DCS system yielded a mean value of $81.42 \pm 0.14 \text{ } \mu\text{s}$, demonstrating highly accurate τ_c measurements, with an error of just 0.00037% relative to the benchmark (the error rate = $\left| \frac{\overline{\tau_{c,SPAD}} - \tau_{c,APD}}{\tau_{c,APD}} \right|$). The significantly lower standard deviation in the ATLAS-DCS system ($0.14 \text{ } \mu\text{s}$ versus $81.39 \text{ } \mu\text{s}$ for the conventional DCS system) indicates a far tighter control and precision in ATLAS-DCS measurements. Also, the SNR was calculated as $\text{mean}(\tau_c)/SD(\tau_c)$ for both systems here, where $SD(\cdot)$ is the standard deviation. The SNRs for APD- and ATLAS-DCS systems were 1 and 571.4, respectively. The proposed ATLAS-DCS system offers a 571-fold enhancement in SNR.

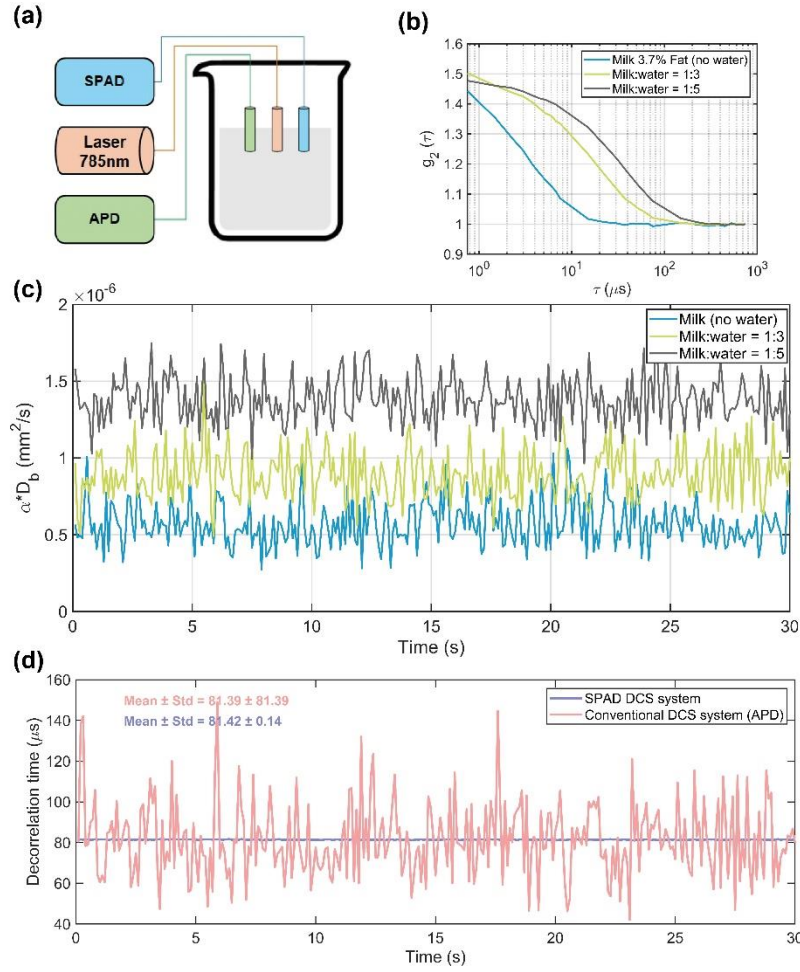


Fig. 4. Validation experiments with milk-phantom and comparative results from the conventional and the ATLAS-DCS systems. (a) The experimental setup with a milk phantom connected to DCS systems at $\rho = 20$ mm. (b) $g_2(\tau)$ for various milk-water dilution ratios (pure milk: 3.7% fat; milk: water = 1:3; milk: water = 1:5 by volume), reflecting changes in light scattering properties with dilution. (c) Temporal variations in αD_b across dilutions, showing reduced diffusion with increasing water content. (d) The decorrelation times for SPAD and conventional DCS systems, with mean and standard deviation values showing the ATLAS-DCS system's superiority.

To further evaluate the conventional DCS system, we measured pulsatile blood flow on the human forehead. The measurement was taken at a sampling rate (fs) of 1 Hz and 10 Hz to assess the system's performance. Figs. 5(a) and (c) show $g_2(\tau)$ at $fs = 1$ Hz (green) and $fs = 10$ Hz (red) for $\rho = 10$ mm and $\rho = 20$ mm respectively. Obviously, the g_2 curve at $fs = 10$ Hz shows more details than that at $fs = 1$ Hz, evident from noisier g_2 at a higher fs . The corresponding decorrelation speed (ν) of Figs. 5(a) and (c), extracted from $g_2(\tau)$ using exponential fitting with Eq. (5), is shown in Figs. 5(b) and (d). These figures illustrate the temporal evaluation of ν over a 10 s window for $\rho = 10$ mm and $\rho = 20$ mm. At $\rho = 10$ mm, the ν at $fs = 10$ Hz (red) resolves more pulsatile signal details than that at $fs = 1$ Hz (green), showing more prominent peaks. However, at $\rho = 20$ mm, $fs = 10$ Hz becomes less pronounced, suggesting that the impact of a higher fs diminishes with an increased measurement depth. The results indicate that a higher fs of 10 Hz offers a more detailed g_2 and ν , particularly at a shallower depth (e.g., $\rho = 10$ mm). This allows better resolving fast BF dynamics, which is critical for applications requiring a high temporal resolution, such as monitoring rapid

physiological changes. However, the increased noise at $f_s = 10$ Hz must be balanced against the desired resolution. At a greater ρ (e.g., 20 mm or 30 mm), the difference in data quality between $f_s = 1$ Hz and $f_s = 10$ Hz is less significant, which means the conventional DCS system is unable to capture BF signals regardless of f_s .

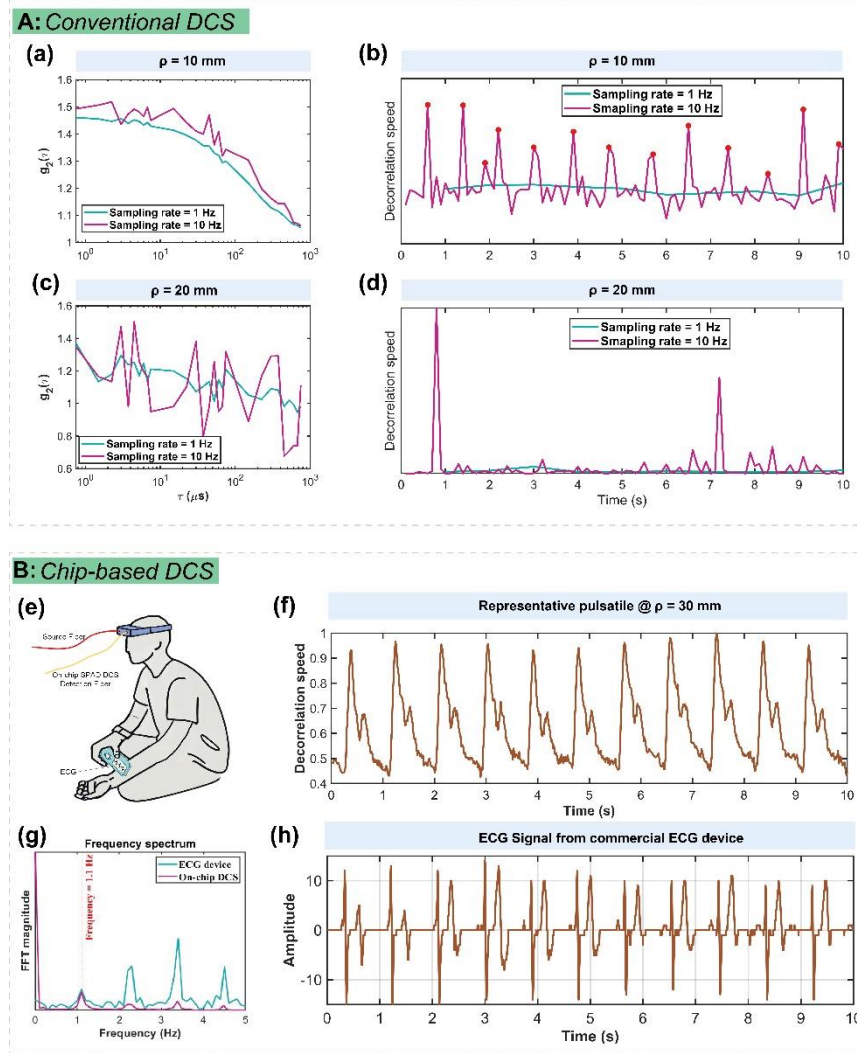


Fig. 5. Human forehead pulse measurements from conventional and ATLAS-DCS systems. **A:** The conventional DCS system; (a) and (c) are for $g_2(\tau)$ at $f_s = 1$ Hz (green) and $f_s = 10$ Hz (red) at $\rho = 10$ mm and $\rho = 20$ mm, respectively. (b) and (d) are the decorrelation speed, extracted from $g_2(\tau)$ after exponential fitting using Eq. (5). **B:** The ATLAS-DCS system; (e) The measurements setup with an ECG device and the ATLAS-DCS system. (f) ATLAS-DCS pulse measurements over 10 s, represented by the normalised decorrelation speed, extracted from autocorrelation curves rate of 13.107ms (4096 iterations) at $f_s = 76$ Hz. (h) The ECG signal acquired from a commercial pulse meter (EMAY, Hongkong, China). (g) The Fourier transform of the DCS pulse and ECG pulse signals.

Similarly, to validate the ATLAS-DCS system, we conducted an experiment measuring the pulse rate on a healthy volunteer's forehead. Figure 5B compares the ATLAS-DCS system against a reference electrocardiogram (ECG) device. The evaluation included time series and frequency domain analysis to assess the ATLAS-DCS system's performance. Fig. 5(f) shows the normalized v from the ATLAS-DCS system, representing a pulsatile BF over a 10 s period at $\rho = 30$ mm. The data, derived from g_2 , was sampled at 13.107 ms intervals over a total of

4096 iterations, and it shows a clear BF curve corresponding to cardiac cycles, as indicated by the recurring peaks that align with physiological pulsations.

For comparison, Fig. 5(h) presents the ECG signal recorded concurrently using a commercial portable pulse meter (EMAY, Ltd., Hong Kong, China). The ECG signal, with its characteristic peaks reflecting the heart's electrical activity, serves as a reference for our DCS measurements. The setup for simultaneous measurements is illustrated in Fig. 5(e). A source fiber delivered light to the subject's forehead, while a detection fiber connected to the ATLAS-DCS system collecting scattered photons. An ECG sensor was placed on the subject's arm for reference measurements. Fig. 5(g) shows the frequency spectra (through Fourier transform) of DCS and ECG pulse signals, with both displaying a peak frequency around 1.1 Hz, corresponding to the subject's average heart rate. The close match in the peak frequency confirms the DCS system's ability to accurately capture heart rate dynamics. The minor differences in harmonic frequencies may be due to variations in signal acquisition and sensitivity to physiological noise.

3.2 Cuff Occlusion

The cuff occlusion measurements were also performed to evaluate the ATLAS-DCS system's performance. The experimental setup is illustrated in Fig. 6(a), where a blood pressure cuff connected to a sphygmomanometer to induce occlusion on a subject's arm. To ensure consistency, we designed a custom fiber holder (3D-printed in-house) hosting a source fiber and two detection fibers – one SMF directing light to an APD for the conventional DCS system and one MMF guiding light to the SPAD array for the ATLAS-DCS system. This configuration enabled simultaneous, *in-vivo* BF measurements, as shown in Fig. 6(c).

We monitored deep tissue BF in a healthy volunteer's arm during an arm-cuff occlusion test. The measurement started at the baseline (0 - 30 s), followed by a cuff-induced occlusion phase (30 - 60 s), where the cuff pressure rapidly increased from 0 to 220 mmHg, and the recovery phase (60 - 90s). The time-course data for the relative blood flow index (rBFi) at $p = 20$ mm and $p = 30$ mm are presented in Figs. 6(b) and (d), respectively. In both figures, the blue curves represent rBFi measurements from the ATLAS-DCS system, whereas the red curves show the results from the conventional DCS system. During the occlusion phase, the ATLAS-DCS system can detect a remarkable decrease in rBFi at $p = 20$ mm and $p = 30$ mm due to reduced BF, and the post-occlusion recovery phase is characterized by a gradual increase in rBFi as the BF level is restored. In contrast, for the conventional DCS system, we only can see it at $p = 20$ mm. The zoomed-in insets of Figs. 6(b) and (d) provide a detailed view of the rBFi fluctuations between 10 and 20 s, highlighting the sensitivity of both systems to pulsatile BF variations. Although a similar trend and the hyperemia peak are observed at $p = 20$ mm and $p = 30$ mm, it is difficult to visualize the heartbeat and dicrotic notch in the conventional DCS system, as shown in the zoomed-in rBFI plots in Figs. 6(b) and (d).

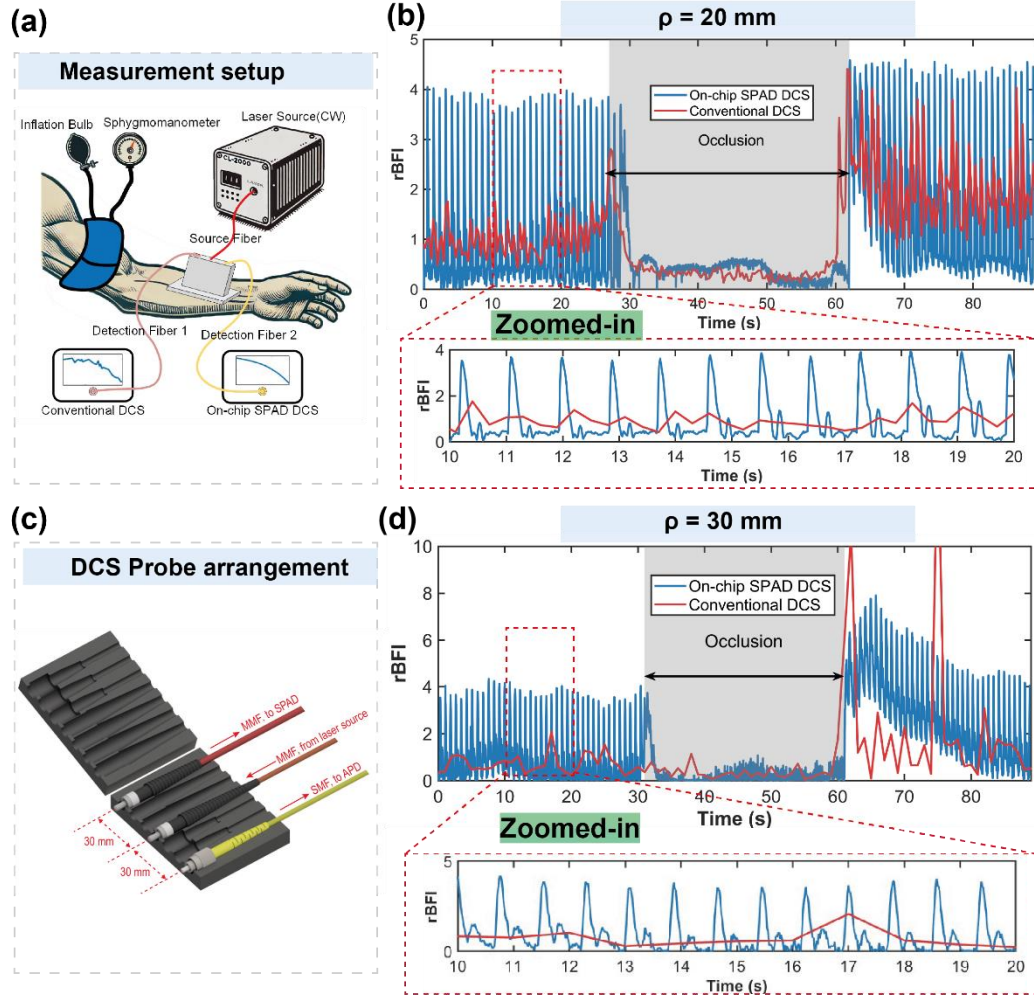


Fig. 6 (a) The cuff occlusion measurement set up. (b) and (d). A comparison between the traditional DCS (red curves) and the SPAD-DCS (blue curves) systems at $\rho = 20$ mm and $\rho = 30$ mm. The graph shows rBFI (relative blood flow index) variations from 0 to 30 s, followed by a simulated occlusion event from 30 to 60 seconds. The inset also provides a zoomed-in view of rBFI fluctuations between 10 and 20 s, highlighting more detailed changes. (c) The schematic diagram of the optical fiber setup in our DCS probe. The diagram shows the arrangement of multimode fibers (MMF), and single-mode fibers (SMF) used in a compact configuration. The MMF (red) directs light to the SPAD, another MMF carries light from the laser source, and the SMF (yellow) directs light to the APD.

3.3. In Vivo Forehead Measurement

Fig. 7 presents cardiac measurements at $\rho = 20, 30, 35, 40, 45$, and 50 mm using the ATLAS-DCS system. The measurements were performed on a healthy volunteer and v , representing BF dynamics, was analysed alongside the corresponding frequency spectra derived from Fast Fourier Transform (FFT). v over a 10-second period is plotted for $\rho = 20, 30$, and 35 mm. The periodic peaks, marked by red dots, correspond to the systolic phase of the cardiac cycle, indicating the pulsatile BF nature. As ρ increases from 20 mm to 35 mm, v maintains its periodicity, though a slight attenuated peak amplitude is observed, likely due to the increased measurement depth and signal attenuation. The corresponding FFT frequency spectrum reveal distinct peaks in the 1-1.5 Hz range, corresponding to the heart rate. The consistency of these peaks across different ρ values validates the system's ability to capture cardiac dynamics at

various depths. The minor peaks at higher frequencies could be attributed to harmonics of the heart rate or physiological noise.

Fig. 7 (b) shows v and corresponding FFT spectra for $\rho = 40, 45$, and 50 mm. At $\rho = 40$ or 45 mm, the systolic peaks are still discernible, although the signals become noisier than that at a smaller ρ . This increased noise is due to deeper penetration into tissue, where scattering events increase, causing a reduced SNR. For $\rho = 50$ mm, v significantly degrades the signal quality, and the pulsatile pattern is no longer clearly visible. This suggests that, at a greater depth, the ATLAS-DCS system struggles to maintain clear detection of BF dynamics due to increased scattering and absorption within the tissue. The frequency spectrum for $\rho = 50$ mm also exhibits diminished signal clarity with no prominent peaks corresponding to the heart rate, indicating that the system's ability to resolve cardiac signals becomes limited at this depth. We will further optimise the sensor in the future to improve the penetration depth.

Compared with the largest ρ in previously reported DCS systems^{43,60}, our ATLAS-DCS system offers higher signal quality, which is apparent from distinct diastole notch and systole peak features in every pulse for $\rho = 20 \sim 50$ mm, as shown in Fig. 7 (c). During diastole, the blood volume in the peripheral tissue compartments is at the lowest level of the cardiac cycle, resulting in decreased absorption from haemoglobin and an increased measured intensity on the detector. In addition, the BF exhibits its minimum value, reducing v of the speckle fluctuations measured by the detector. Conversely, during systole, the blood volume reaches its maximal, resulting in increased haemoglobin and a decreased measured intensity.

The boxplot in Fig. 7(d) shows τ_c as a function of $\rho = 20 \sim 50$ mm. As ρ increases, τ_c decreases reflecting a reduced signal strength. At a smaller ρ , for example at $\rho = 20$ mm, τ_c shows a larger standard deviation with a median above $150 \mu s$, indicating stronger and more varied blood flow signals when probing shallower tissues. As ρ increases, the interquartile range shrinks significantly, and the median τ_c gradually decreases, reaching around $75 \mu s$ at $\rho = 50$ mm. This behaviour suggests that deeper tissue exhibits a lower decorrelation time due to the proportion of mixed dynamic and static signals increases. The dynamics in deeper tissues are faster and signal weakens, leading to a shorter τ_c .

SNR Calculation

The SNR of v was calculated by first identifying each pulse peak using Matlab's *findpeaks* function, then dividing the mean peak value by the peak value's standard deviation. Fig. 7(e) demonstrates that the SNR versus ρ ; SNR decreases as ρ increases. At $\rho = 20$ mm, the SNR reaches its maximal, around 45 (a.u.), reflecting strong signal detection due to the proximity to superficial BF. However, as ρ increases to 50 mm, the SNR declines sharply to approximately 10 (a.u.), indicating a significant degradation in signal quality. The observed decline in SNR agrees with the trend in τ_c (as shown in Fig. 7(d)), where a larger ρ leads to a lower τ_c and increased noise. The reduced SNR at a larger ρ can be attributed to increased photon scattering and absorption, reducing BF detection efficiency from deeper tissue. These results highlight the trade-off between ρ and signal integrity.

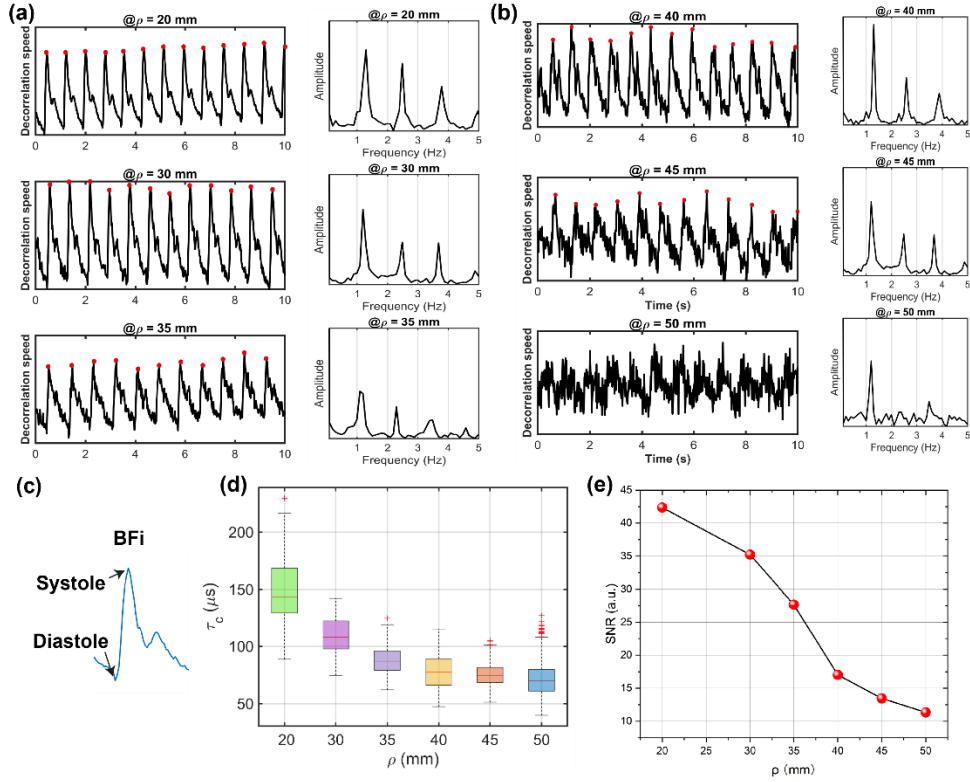


Fig. 7 (a) Cardiac measurements at $\rho = 20$ to 50 mm. (a) n curves at $\rho = 20$ to 35 mm and corresponding frequency spectra. The red dots in the subgraph of n plots stand for systolic timepoints. (b) n curves at $\rho = 40$ to 50 mm and corresponding frequency spectra. The results were obtained from a healthy subject using ALTAS-DCS system. (c) A representative example of BFi fluctuations, illustrating systolic and diastolic phases. (d) Boxplots of τ_c distributions at different ρ . (e) SNR versus ρ .

3.4. Human Prefrontal Cortex Activation Test

The prefrontal cortex is responsible for cognitive functions such as planning, thinking, working memory, and cognitive processes and decision-making during an active task requiring attention and coordination⁶¹. To further assess the ALTAS-DCS system's functionality, we conducted a prefrontal cortex activation test while the subject engaged in a video game (**Brawl Stars**). The objective was to monitor CBF variations within the prefrontal cortex. To reduce the effects of superficial layers we set $\rho = 30$ mm⁶². Fig. 8(b) shows the continuous decorrelation time measurements over a period of 177 s from a subject. The blue and red shaded regions represent different test stages: the baseline (blue) where the subject was in a resting state, the video game playing phase (red), and the post-task resting state (blue). $g_2(\tau)$ and τ_c were calculated using an integration time of 5.24 ms (4096 iterations) under the DCS ensemble mode (with $PixClk = 25$ MHz). During the gameplay phase, there is a notable decrease in τ_c , indicating elevated neural activity in the prefrontal cortex and corresponding to greater blood flow. In the post-phase τ_c returns to its resting state. To better see the trend, we estimated τ_c 's mean ($\bar{\tau}_c$) and τ_c 's standard deviation (σ_{τ_c}) every 10 seconds. Fig. 8(c) shows the average τ_c for each state (thin blue line), $\bar{\tau}_c$ (thick blue/red lines or solid horizontal line), and $\bar{\tau}_c \pm \sigma_{\tau_c}$ (banded curve) for three different states. $\bar{\tau}_c$ was relatively stable for $46.7 \mu s$, before the participant engaged in the video game ($\bar{\tau}_c = 43.4 \mu s$) and returned to the resting stage ($\bar{\tau}_c = 44.2 \mu s$).

This trend reflects the heightened brain activity and increased CBF due to the cognitive load induced by the video game, matching previously reported results^{39,62}.

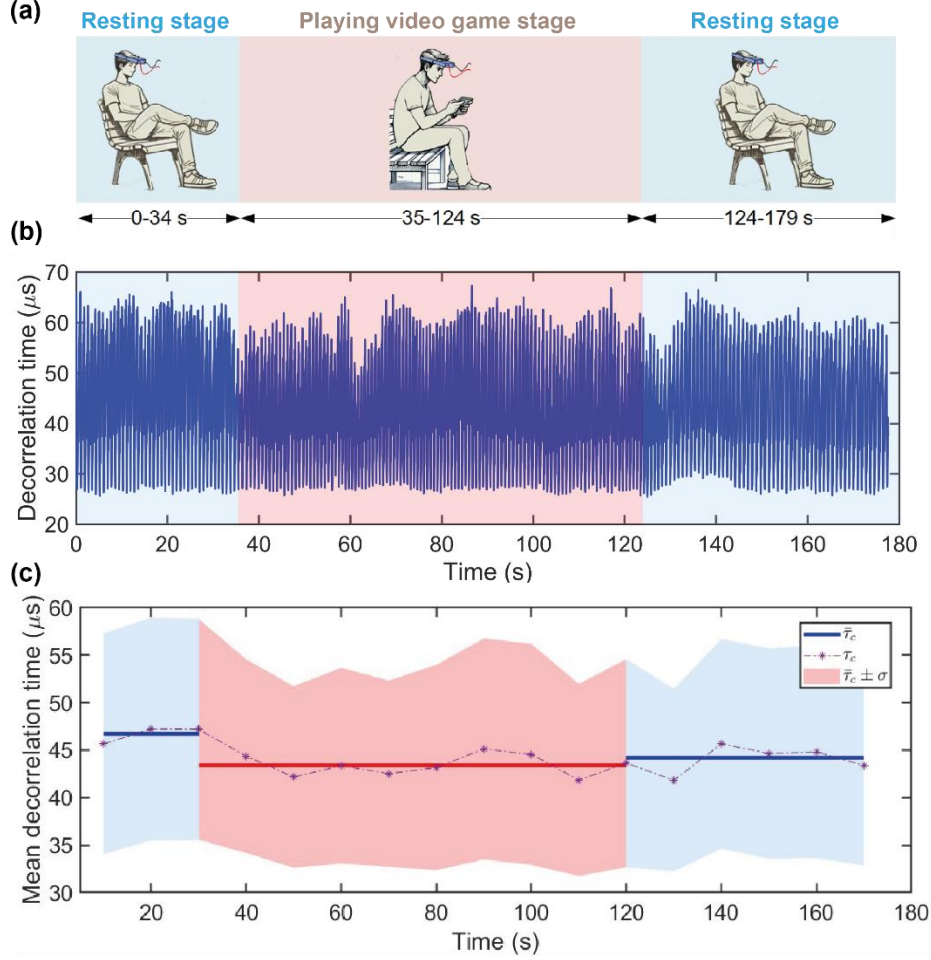


Fig. 8. The experimental setup and human prefrontal cortex activation tests. (a) The schematic diagram of measurements. (b) The τ_c plot over a period of 177 seconds including two resting and one video-gamer playing stages. (c) $\bar{\tau}_c + \sigma_{\tau_c}$ of every 10 s of τ_c . Solid horizontal lines represent the average decorrelation of each stage.

4. Discussions

This study presents an ATLAS-DCS system with on-chip autocorrelators operating in the ensemble mode at varied clock rates ($PixClk = 10$ MHz or 25 MHz). ATLAS contains a 512×512 SPAD array (arranged in 128×128 macropixels, embedded with 128×128 autocorrelators (DCS imaging mode)⁵⁰, which allowed obtaining g_2 that average over thousands of independent speckle fluctuation measurements per frame to improve the system sensitivity and speed (in the ensemble mode). Unlike previously published FPGA-based autocorrelators⁴⁸ to reach a measurement rate of 50 Hz, our ATLAS-DCS system can achieve fast and accurate analysis at a measurement rate of 56.3 Hz, suitable for real-time applications. The on chip autocorrelators enhances data throughput and offers real-time analysis, facilitating broad applications. We used this ATLAS-DCS system to measure BFi waveforms from human forearms and foreheads with a 13.3 ms temporal resolution and detect behavior induced variations from the prefrontal cortex.

Highly integrated CMOS SPAD arrays were boosted first by 3D/time-resolved fluorescence imaging applications^{63–65}, and later Richardson *et al.*'s⁶⁶ low noise SPAD structures emerged from the EU6 MEGAFRAME project⁶⁷. These SPAD arrays contain either time-correlated single-photon counting (TCSPC)^{68–70} or time-gating modules^{71,72}. Since Johansson *et al.* presented the first SPAD-DCS system using a 5×5 SPAD array³⁸ in 2019, SPAD arrays have been used in multispeckle DCS systems to enhance the SNR. More details about the evolution of SPAD-based DCS systems with an enhanced SNR gain from 1~500 were revealed in Ref. ²³. Recent advances in 3D-stacks backside illumination technologies⁷³ allow fully enhancing the imager fill factor and higher NIR PDE. These improvements collectively allow blood flow measurements at a larger ρ ⁴⁴. Compared with on-chip solutions, FPGAs-based autocorrelator^{41,48,74–77} have been investigated for years. Recently, Moore *et al.*⁴⁸ from Lin's group implemented an FPGA-based DCS system achieving fast and accurate DCS analysis. Another advantage of FPGA-based DCS systems is that it can provide a high number of DCS bins. However, they have higher power consumption in the chip and within the FPGA-based autocorrelators due to high I/O rates and computations required. In addition, FPGA-based autocorrelators usually employ a multi-tau approach, requiring multiple clocks and accumulators between shift registers crossing clock boundaries^{44,74}. Embedding autocorrelators with the sensor breaks the I/O bottleneck between the sensor and FPGA, leading to increased frame rates and hugely reducing the power consumption. Additionally, having smaller form-factor, embedded autocorrelators provide a pathway to multiplexed and wearable DCS systems.

The milk-phantom experiment results show that our ATLAS-DCS system performs much better than the reference DCS system (APD-based). The conventional DCS system's ability to detect pulsatile blood flow and characterize dynamic changes in blood velocity is demonstrated in Fig. 4. The sampling rate plays a crucial role in the resolution and measurement noise. These findings are important for optimizing the DCS systems based on the depth of interest and the required temporal resolution for a specific clinical application.

From Fig. 5, our system shows strong agreement with the reference ECG data in time and frequency domains. The DCS system's ability to track the decorrelation speed dynamics, showcasing its potential for non-invasive, real-time monitoring of cerebral and peripheral blood flow. Fig. 6 shows the ATLAS-DCS system's superior performances in rBFI measurements against traditional DCS systems. Both systems captured similar trends in blood flow dynamics during the baseline, occlusion, and recovery phases. However, the ATLAS-DCS system provides a higher sensitivity to rapid blood flow variations, as evidenced by the sharper transitions during onset and recovery, particularly at $\rho = 20$ mm. This higher sensitivity is desirable for applications requiring real-time monitoring of dynamic physiological changes.

From Fig. 7, the ATLAS-DCS system can capture pulsatile blood flow for $\rho = 50$ mm, with the clearest signals observed at $\rho = 20$ to 35 mm. As ρ increases, the signal quality degrades due to the increased optical path length, leading to greater scattering and a reduced SNR. The FFT analysis supports these observations, showing well-defined peaks at heart rate frequencies for $\rho = 45$ mm but a lack of clear frequency components at $\rho = 50$ mm. These findings suggest that while the system performs well at shallow to intermediate depths, improvements in signal processing or hardware may be required to extend its performance to deeper tissue

measurements. Nonetheless, the ATLAS-DCS system demonstrates promising potential for non-invasive, real-time monitoring of blood flow in clinical and research applications, particularly for $\rho = 20 \sim 45$ mm. The observed increase in τ_c during the gameplay phase aligns with expected physiological changes, such as an increased CBF level in response to more cognitive demands. This demonstrates the ATLAS-DCS system's capacity in real-time monitoring brain activity. The system can also detect transitions between active and resting states with high sensitivity. These results show the potential of using the ATLAS-DCS system for non-invasive monitoring of cerebral hemodynamics in cognitive tasks and brain functions.

5. Conclusion

We have characterized the ATLAS-DCS system for assessing CBF up to $\rho = 50$ mm, benefited from on-chip embedded autocorrelators. It offers real-time blood flow monitoring (see the video in Supplementary) at a 56 Hz sampling rate while maintaining the accuracy and performing better than a conventional APD-based DCS system. We demonstrated that the device could assess cerebrovascular reactivity. We believe that it has potential applications in assessing cerebrovascular diseases and in brain research.

Acknowledgements

The authors extend their gratitude to the Diffuse Correlation Spectroscopy (DCS) community for the valuable discussions and collaborations over the past two years, particularly with esteemed scholars from Linköping University, Harvard Medical School, Western University, Duke University, Boston University, and Singapore A*STAR. We are especially grateful to Johannes D. Johansson, Stefan A. Carp, and Renzhe Bi for their insightful discussions that contributed to this work. Additionally, we acknowledge Saeed Samaei, Mamadou Diop, Lucas Kreiss, Byungehan Kim, Wenhui Liu, Tom Y. Cheng, Mitchell B. Robinson and Xiaojun Chen for their valuable discussions in the field of diffuse optics over the past two years. ATLAS was designed in a project funded by Reality Labs, Meta Platforms Inc., Menlo Park, CA 94025, USA. We are grateful to STMicroelectronics for CMOS manufacturing of the device within the University of Edinburgh Collaboration Agreement.

Subjects. Four subjects within 20 to 35 years of age with no prior diagnosis or treatment of neurological disorders were recruited for this study. Sex, gender, race, and ethnicity were not considered during recruitment. Subjects were recruited through on-department advertisements. Three subjects were recruited for the cuff occlusion measurement, and one was recruited to measure CBF changes by behaviour-induced physiological variations from the subject's prefrontal cortex during video gaming. The experimental procedure and protocols were approved and carried out by the regulations of the Institutional Review Board at the University of Strathclyde. Each participant provided a signed written informed consent form before the experiment.

Statistics. The SNR of v was calculated by first identifying each pulse peak using MATLAB's *findpeaks* function, then dividing the mean peak value by the standard deviation of the peak values while investigating the SNR between ρ using the ATLAS-DCS system.

Data and Code Availability

All datasets and codes supporting the findings of this study are available from the corresponding author upon reasonable request.

Author Contributions

Q. W. conceived the presented idea, designed the optical setup, and performed the analysis. Q. W., C. L., M. P., and Y. Z. carried out the experiments and contributed to the analysis and interpretation of the results. Y. H., M. W., A. E., A. G., N. F., and R. H. provided technical support in ATLAS. D. L. devised and supervised the project and the findings of this work. All authors contributed to the writing of this paper.

Competing interests

The authors declare no competing interests.

Funding

This work has been funded by the Engineering and Physical Sciences Research Council (Grant No. EP/T00097X/1 and No. EP/T020997/1); the Quantum Technology Hub in Quantum Imaging (QuantiC) and the University of Strathclyde.

Supplementary Material

Supplementary video

A video showing the real time cuff Occlusion *in vivo*

References

1. Raichle, M. E. & Mintun, M. A. BRAIN WORK AND BRAIN IMAGING. *Annu. Rev. Neurosci.* **29**, 449–476 (2006).
2. Fan, J.-L. *et al.* Integrative cerebral blood flow regulation in ischemic stroke. *Journal of Cerebral Blood Flow & Metabolism* **42**, 387 (2021).
3. Bandera, E. *et al.* Cerebral Blood Flow Threshold of Ischemic Penumbra and Infarct Core in Acute Ischemic Stroke. *Stroke* **37**, 1334–1339 (2006).
4. Yun, J.-H. A Brief Introduction to the Study of Cerebral Blood Flow Measurement in Traumatic Brain Injury Using Optical Imaging Approach. *Korean Journal of Neurotrauma* **20**, 5 (2024).
5. Khellaf, A., Khan, D. Z. & Helmy, A. Recent advances in traumatic brain injury. *J Neurol* **266**, 2878–2889 (2019).
6. Sweeney, M. D., Kisler, K., Montagne, A., Toga, A. W. & Zlokovic, B. V. The role of brain vasculature in neurodegenerative disorders. *Nat Neurosci* **21**, 1318–1331 (2018).
7. Alzheimer's: reduced cerebral blood flow plays a central role in the disease's development | CNRS. <https://www.cnrs.fr/en/press/alzheimers-reduced-cerebral-blood-flow-plays-central-role-diseases-development> (2019).
8. Goldsmith, H. S. Alzheimer's Disease: A Decreased Cerebral Blood Flow to Critical Intraneuronal Elements Is the Cause. *Journal of Alzheimer's Disease* **85**, 1419 (2022).
9. Firbank, M. J., Colloby, S. J., Burn, D. J., McKeith, I. G. & O'Brien, J. T. Regional cerebral blood flow in Parkinson's disease with and without dementia. *NeuroImage* **20**, 1309–1319 (2003).
10. Arslan, D. B. *et al.* The cerebral blood flow deficits in Parkinson's disease with mild cognitive impairment using arterial spin labeling MRI. *J Neural Transm* **127**, 1285–1294 (2020).

11. Cheng, X., Sie, E. J., Naufel, S., Boas, D. A. & Marsili, F. Measuring neuronal activity with diffuse correlation spectroscopy: a theoretical investigation. *Neurophoton.* **8**, (2021).
12. Durduran, T. *et al.* Diffuse optical measurement of blood flow, blood oxygenation, and metabolism in a human brain during sensorimotor cortex activation. *Opt. Lett.* **29**, 1766 (2004).
13. Jaillon, F., Li, J., Dietsche, G., Elbert, T. & Gisler, T. Activity of the human visual cortex measured non-invasively by diffusing-wave spectroscopy. *Opt. Express, OE* **15**, 6643–6650 (2007).
14. Boas, D. A. DIFFUSE PHOTON PROBES OF STRUCTURAL AND DYNAMICAL PROPERTIES OF TURBID MEDIA: THEORY AND BIOMEDICAL APPLICATIONS.
15. Boas, D. A., Campbell, L. E. & Yodh, A. G. Scattering and Imaging with Diffusing Temporal Field Correlations. *Phys. Rev. Lett.* **75**, 1855–1858 (1995).
16. Fredriksson, I., Fors, C. & Johansson, J. Laser Doppler Flowmetry – A Theoretical Framework. (2012).
17. Senarathna, J., Rege, A., Li, N. & Thakor, N. V. Laser Speckle Contrast Imaging: theory, instrumentation and applications. *IEEE Rev Biomed Eng* **6**, 99–110 (2013).
18. Bi, R., Dong, J. & Lee, K. Deep tissue flowmetry based on diffuse speckle contrast analysis. *Opt. Lett.* **38**, 1401 (2013).
19. Bi, R. *et al.* Fast pulsatile blood flow measurement in deep tissue through a multimode detection fiber. *J. Biomed. Opt.* **25**, 1 (2020).
20. Valdes, C. P. *et al.* Speckle contrast optical spectroscopy, a non-invasive, diffuse optical method for measuring microvascular blood flow in tissue. *Biomed. Opt. Express* **5**, 2769 (2014).
21. Kim, B. *et al.* Measuring human cerebral blood flow and brain function with fiber-based speckle contrast optical spectroscopy system. *Commun Biol* **6**, 1–10 (2023).

22. Mesquita, R. C. *et al.* Direct measurement of tissue blood flow and metabolism with diffuse optics. *Phil. Trans. R. Soc. A.* **369**, 4390–4406 (2011).
23. Wang, Q. *et al.* A comprehensive overview of diffuse correlation spectroscopy: Theoretical framework, recent advances in hardware, analysis, and applications. *NeuroImage* **298**, 120793 (2024).
24. Durduran, T. & Yodh, A. G. Diffuse correlation spectroscopy for non-invasive, micro-vascular cerebral blood flow measurement. *NeuroImage* **85**, 51–63 (2014).
25. Yu, G. Near-Infrared Diffuse Correlation Spectroscopy (DCS) for Assessing Deep Tissue Blood Flow. *Anatom Physiol* **02**, (2012).
26. Near-Infrared Diffuse Correlation Spectroscopy for Assessment of Tissue Blood Flow. in *Handbook of Biomedical Optics* (eds. Boas, D. A., Pitris, C. & Ramanujam, N.) 215–236 (CRC Press, 2016). doi:10.1201/b10951-14.
27. Buckley, E. M., Parthasarathy, A. B., Grant, P. E., Yodh, A. G. & Franceschini, M. A. Diffuse correlation spectroscopy for measurement of cerebral blood flow: future prospects. *Neurophoton* **1**, 011009 (2014).
28. Baker, W. B. *et al.* Continuous non-invasive optical monitoring of cerebral blood flow and oxidative metabolism after acute brain injury. *J Cereb Blood Flow Metab* **39**, 1469–1485 (2019).
29. Poon, C.-S. *et al.* Noninvasive Optical Monitoring of Cerebral Blood Flow and EEG Spectral Responses after Severe Traumatic Brain Injury: A Case Report. *Brain Sciences* **11**, 1093 (2021).
30. Selb, J. *et al.* Prolonged monitoring of cerebral blood flow and autoregulation with diffuse correlation spectroscopy in neurocritical care patients. *Neurophoton.* **5**, 1 (2018).

31. Yazdi, H. S. *et al.* Mapping breast cancer blood flow index, composition, and metabolism in a human subject using combined diffuse optical spectroscopic imaging and diffuse correlation spectroscopy. *J Biomed Opt* **22**, 045003 (2017).
32. Sunar, U. Monitoring photodynamic therapy of head and neck malignancies with optical spectroscopies. *World J Clin Cases* **1**, 96–105 (2013).
33. Sunar, U. *et al.* Hemodynamic responses to antivasular therapy and ionizing radiation assessed by diffuse optical spectroscopies. *Opt. Express* **15**, 15507 (2007).
34. Sunar, U. *et al.* Monitoring photobleaching and hemodynamic responses to HPPH-mediated photodynamic therapy of head and neck cancer: a case report. *Opt. Express* **18**, 14969 (2010).
35. Zhou, C. *et al.* Diffuse optical monitoring of blood flow and oxygenation in human breast cancer during early stages of neoadjuvant chemotherapy. *JBO* **12**, 051903 (2007).
36. Dietsche, G. *et al.* Fiber-based multispeckle detection for time-resolved diffusing-wave spectroscopy: characterization and application to blood flow detection in deep tissue. *Appl Opt* **46**, 8506–8514 (2007).
37. Carp, S. A., Robinson, M. B. & Franceschini, M. A. Diffuse correlation spectroscopy: current status and future outlook. *Neurophotonics* **10**, 013509 (2023).
38. Johansson, J. D., Portaluppi, D., Buttafava, M. & Villa, F. A multipixel diffuse correlation spectroscopy system based on a single photon avalanche diode array. *Journal of Biophotonics* **12**, e201900091 (2019).
39. Liu, W. *et al.* Fast and sensitive diffuse correlation spectroscopy with highly parallelized single photon detection. *APL Photonics* **6**, 026106 (2021).
40. Sie, E. J. *et al.* High-sensitivity multispeckle diffuse correlation spectroscopy. *Neurophotonics* **7**, 035010 (2020).

41. Della Rocca, F. M., Sie, E. J., Catoen, R., Marsili, F. & Henderson, R. K. Field programmable gate array compression for large array multispeckle diffuse correlation spectroscopy. *J Biomed Opt* **28**, 057001 (2023).
42. Henderson, R. K. *et al.* A 192×128 Time Correlated SPAD Image Sensor in 40-nm CMOS Technology. *IEEE Journal of Solid-State Circuits* **54**, 1907–1916 (2019).
43. Wayne, M. A. *et al.* Massively parallel, real-time multispeckle diffuse correlation spectroscopy using a 500×500 SPAD camera. *Biomed Opt Express* **14**, 703–713 (2023).
44. Gorman, A. *et al.* ATLAS: A large array, on-chip compute SPAD camera for multispeckle diffuse correlation spectroscopy. *Biomedical Optics Express* (2024)
doi:10.1364/BOE.531416.
45. Rocca, F. M. D. *et al.* A 512×512 SPAD Laser Speckle Autocorrelation Imager in Stacked 65/40nm CMOS. (2024).
46. Wang, D. *et al.* Fast blood flow monitoring in deep tissues with real-time software correlators. *Biomed Opt Express* **7**, 776–797 (2016).
47. Dong, J. *et al.* Diffuse correlation spectroscopy with a fast Fourier transform-based software autocorrelator. *JBO* **17**, 097004 (2012).
48. Moore, C. H., Sunar, U. & Lin, W. A Device-on-Chip Solution for Real-Time Diffuse Correlation Spectroscopy Using FPGA. *Biosensors (Basel)* **14**, 384 (2024).
49. Kreiss, L. *et al.* Beneath the Surface: Revealing Deep-Tissue Blood Flow in Human Subjects with Massively Parallelized Diffuse Correlation Spectroscopy. Preprint at <http://arxiv.org/abs/2403.03968> (2024).
50. Rocca, F. M. D. *et al.* A 512×512 SPAD Laser Speckle Autocorrelation Imager in Stacked 65/40nm CMOS.
51. Boas, D. A. & Yodh, A. G. Spatially varying dynamical properties of turbid media probed with diffusing temporal light correlation. *J. Opt. Soc. Am. A* **14**, 192 (1997).

52. Farrell, T. J., Patterson, M. S. & Wilson, B. A diffusion theory model of spatially resolved, steady-state diffuse reflectance for the noninvasive determination of tissue optical properties *in vivo*. *Med. Phys.* **19**, 879–888 (1992).
53. Ferreira, D., Bachelard, R., Guerin, W., Kaiser, R. & Fouché, M. Connecting field and intensity correlations: The Siegert relation and how to test it. *American Journal of Physics* **88**, 831–837 (2020).
54. Fercher, A. F. & Briers, J. D. Flow visualization by means of single-exposure speckle photography. *Optics Communications* **37**, 326–330 (1981).
55. Cheung, C., Culver, J. P., Takahashi, K., Greenberg, J. H. & Yodh, A. G. In vivo cerebrovascular measurement combining diffuse near-infrared absorption and correlation spectroscopies. *Phys Med Biol* **46**, 2053–2065 (2001).
56. Goodman, J. W. *Speckle Phenomena in Optics: Theory and Applications*. (Roberts and Company Publishers, 2007).
57. Zavriyev, A. I. *et al.* The role of diffuse correlation spectroscopy and frequency-domain near-infrared spectroscopy in monitoring cerebral hemodynamics during hypothermic circulatory arrests. *JTCVS Techniques* **7**, 161 (2021).
58. Aernouts, B. *et al.* Visible and near-infrared bulk optical properties of raw milk. *Journal of Dairy Science* **98**, 6727–6738 (2015).
59. Irwin, D. *et al.* Influences of tissue absorption and scattering on diffuse correlation spectroscopy blood flow measurements. *Biomed. Opt. Express* **2**, 1969 (2011).
60. Kreiss, L. *et al.* Beneath the Surface: Revealing Deep-Tissue Blood Flow in Human Subjects with Massively Parallelized Diffuse Correlation Spectroscopy. Preprint at <http://arxiv.org/abs/2403.03968> (2024).
61. Siddiqui, S. V., Chatterjee, U., Kumar, D., Siddiqui, A. & Goyal, N. Neuropsychology of prefrontal cortex. *Indian Journal of Psychiatry* **50**, 202 (2008).

62. Samaei, S., Nowacka, K., Gerega, A., Pastuszak, Ż. & Borycki, D. Continuous-wave parallel interferometric near-infrared spectroscopy (CW π NIRS) with a fast two-dimensional camera. *Biomed. Opt. Express* **13**, 5753 (2022).
63. Niclass, C., Rochas, A., Besse, P.-A. & Charbon, E. Design and characterization of a CMOS 3-D image sensor based on single photon avalanche diodes. *IEEE J. Solid-State Circuits* **40**, 1847–1854 (2005).
64. Stoppa, D. *et al.* A CMOS 3-D Imager Based on Single Photon Avalanche Diode. *IEEE Trans. Circuits Syst. I* **54**, 4–12 (2007).
65. Mosconi, D., Stoppa, D., Pancheri, L., Gonzo, L. & Simoni, A. CMOS Single-Photon Avalanche Diode Array for Time-Resolved Fluorescence Detection. in *2006 Proceedings of the 32nd European Solid-State Circuits Conference* 564–567 (IEEE, Montreux, 2006). doi:10.1109/ESSCIR.2006.307487.
66. Richardson, J. A., Grant, L. A. & Henderson, R. K. Low Dark Count Single-Photon Avalanche Diode Structure Compatible With Standard Nanometer Scale CMOS Technology. *IEEE Photon. Technol. Lett.* **21**, 1020–1022 (2009).
67. <https://cordis.europa.eu/project/id/029217>.
68. R. K. Henderson, ‘A 192 x 128 Time Correlated SPAD Image Sensor in 40 nm CMOS Technology’.
69. Veerappan, C. *et al.* A 160×128 single-photon image sensor with on-pixel 55ps 10b time-to-digital converter. in *2011 IEEE International Solid-State Circuits Conference* 312–314 (2011). doi:10.1109/ISSCC.2011.5746333.
70. Becker, W., Bergmann, A., Biscotti, G. L. & Rueck, A. Advanced time-correlated single photon counting techniques for spectroscopy and imaging in biomedical systems. in (eds. Neev, J., Schaffer, C. B. & Ostendorf, A.) 104 (San Jose, Ca, 2004). doi:10.1117/12.529143.

71. Li, D.-U. *et al.* Real-time fluorescence lifetime imaging system with a 32×32 $0.13\mu\text{m}$ CMOS low dark-count single-photon avalanche diode array. *Opt. Express* **18**, 10257 (2010).
72. Ulku, A. C. *et al.* A 512×512 SPAD Image Sensor with Integrated Gating for Widefield FLIM. *IEEE J Sel Top Quantum Electron* **25**, 6801212 (2019).
73. Mamdy, B. *et al.* A high PDE and high maximum count rate and low power consumption 3D-stacked SPAD device for Lidar applications. in.
74. Buchholz, J. *et al.* FPGA implementation of a 32×32 autocorrelator array for analysis of fast image series. *Opt. Express, OE* **20**, 17767–17782 (2012).
75. Islambek, A., Yang, K., Li, W. & Li, K. FPGA-based real-time autocorrelator and its application in dynamic light scattering. *Optik* **194**, 163047 (2019).
76. Lin, W., Busch, D. R., Goh, C. C., Barsi, J. & Floyd, T. F. Diffuse Correlation Spectroscopy Analysis Implemented on a Field Programmable Gate Array. *IEEE Access* **7**, 122503–122512 (2019).
77. Moore, C. H. & Lin, W. FPGA Correlator for Applications in Embedded Smart Devices. *Biosensors* **12**, 236 (2022).